Proceedings of ASME Turbo Expo 2003
Power for Land, Sea, and Air
June 16-19, 2003, Atlanta, Georgia USA

GT2003-38933

MICRO-SCALE RADIAL-FLOW COMPRESSOR IMPELLER MADE OF SILICON NITRIDE - MANUFACTURING AND PERFORMANCE -

Sangkyun Kang
Department of
Mechanical Engineering
Stanford University
Stanford, California 94305

James P. Johnston
Department of
Mechanical Engineering
Stanford University
Stanford, California 94305

Toshiyuki Arima
Wako Research Center
Honda R&D Co. Ltd.
Saitama, Japan

Minoru Matsunaga
Wako Research Center
Honda R&D Co. Ltd.
Saitama, Japan

Hideaki Tsuru
Honda Research Institute USA, Inc.
Mountain View, CA 94041

Fritz B. Prinz
Department of
Mechanical Engineering
Stanford University
Stanford, California 94305

ABSTRACT

A micro-scale, high-speed compressor impeller (12 mm diameter, 800,000 rpm) was tested for feasibility in regard to aerodynamic performance. The compressor was designed for application in a fist-sized gas-turbine-generator. To survive high stresses at such high temperatures, the rotor was manufactured as a single turbine/compressor/shaft unit in silicon nitride, by the Mold SDM process. Performance testing was conducted in a cold-flow rig at reduced speed of 420,000 rpm. Results from a CFD code compared favorably to measured data at this speed. Extrapolation from test conditions to full design speed was accomplished by application of CFD applied at both speeds.

Keywords: compressor, micro-scale, CFD, gas turbine engine, SDM

NOMENCLATURE

b_2	Hub to shroud distance at exit station
b_{tip}	Hub to shroud distance at blade tip. Here, $b_2 = b_{tip}$
C_p	Specific heat at constant pressure. Here, $C_p = 1005\ (m^2/s^2K)$
k	Ratio of specific heats. Here, k = 1.4
M_g	Mass flow rate
N	Rotating speed (rpm)
P_c	Collection chamber pressure
P_s	Probability of survival of a ceramic specimen under specified loads
P_f	Probability of failure of a ceramic specimen. Here, $P_f = 1 - P_s$
P_2	Static pressure at (2)
Po_1	Inlet total and static pressure, Here, 1 atm = 101.4 kPa
Po_2	Total pressure at (2)
R	Gas constant. Here, R = 287 (N-m/kg-K)
R_2	Radius of exit station (6.9 mm)
R_{tip}	Radius of the rotor at tip
ω	Rotating speed (1/sec)
T_2	Static temperature at (2)
To_1	Total temperature at (1). Range = 289 to 296 K
To_2	Total temperature at (2)
U_{tip}	Rotor tip speed: ωR_{tip}
V_{r2}	Radial flow speed at (2)

V_{t2}	Tangential flow speed at (2)
$V_{t_{tip}}$	Tangential flow speed at tip
η	Adiabatic efficiency, see Equation 8
ρ_2	Static density at (2)
σ_{max}	maximum stress

INTRODUCTION

The need for a portable micro-sized power source is increasing with the development of unmanned aerial vehicles, autonomous robots and other mobile devices. Since it is known that the power density of a gas turbine engine is inversely proportional to its length scale, a gas turbine engine with a rotary generator was chosen over other possible devices [1, 2]. In this paper, the compressor for the gas turbine engine is the principal object of investigation.

Preliminary design analysis showed that a gas-turbine-generator based on a simple Brayton cycle with a cycle pressure ratio of 3:1 could produce the desired power in a fist-sized package, excluding fuel tank and controls. The largest component is a reverse flow annular combustion chamber. The radial flow compressor and turbine rotors are much smaller. They are mounted back-to-back in an overhung configuration on the shaft, ahead of the rear bearing. The generator, mounted between the front and rear bearings, is the second largest component of the package.

With rotors of 12 mm diameter, the shaft must spin at 800,000 rpm (500 m/s tip speed) to achieve the design pressure ratio of 3:1 using a radial flow compressor impeller with backward leaning blades. To withstand the high stresses at high temperature without the need for auxiliary cooling, a ceramic material was chosen for the rotors and shaft. Also, to achieve the desired performance levels, the turbine and compressor were designed with the fully three-dimensional geometry obtained in conventional turbomachines. These geometric criteria were achieved by the use of Mold SDM process, developed in the Rapid Prototyping Laboratory at Stanford University, to produce very small, intricate, three-dimensional rotors and shafts out of silicon nitride.

The compressor rotor, Figure 1, was designed to be about 12 mm in diameter with unshrouded blades. It had 6 full blades and 6 partial blades (splitters) which inclined backwards at approximately 50 degrees at the tip. The hub-to-shroud depth at the tip, diffuser inlet, was about 1 mm, and the axial tip clearance was 76 μm. At design point flow rate of 2.38 g/s, a work input coefficient ($V_{t_{tip}}/U_{tip}$) of about 0.7 was utilized so that the impeller would have enough pressure rise to produce a stage pressure ratio of 3.0 and efficiency of 65 %. Loss estimates used in the preliminary design included low Reynolds number effects plus a tip clearance leakage loss of 4 %.

Downstream of the impeller, a thin-vaned, radial flow diffuser, proceeded by a short vaneless space, was designed for use in the actual engine. In the study presented here, a vaneless diffuser (1 mm deep with a radius ratio of 2:1) ahead of an exit dump chamber was used for the experiments and for the computational fluid dynamics (CFD) which were intended to explore the performance of the impeller.

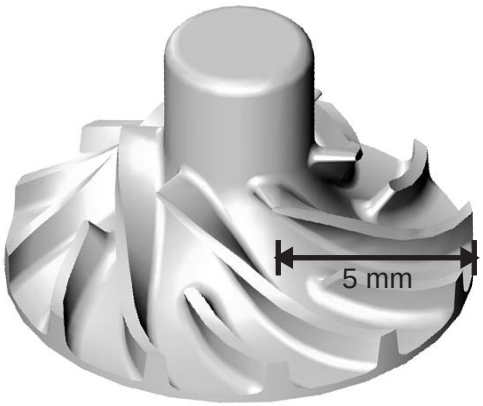

Figure 1. CAD model of compressor

Many technical hurdles remain in the design of the final power plant. For example, the type of bearings is a major issue. Air journal and thrust bearings were employed in the 4 mm diameter rotors of the 10 Watt micro gas turbine generator developed at the MIT Gas Turbine Laboratory [2]. They were also used in the 10 mm rotors of the 100 Watt engine design by IHI and Tohoku University [3]. Modern developments in ball bearings for high speeds and small sizes, such as those used in air-turbines for dental drills, may also offer an option. For our work, we employed ball bearings for the compressor impellers which were tested up to 420,000 rpm (260 m/s tip speed). In separate tests in a special, small bearing test stand which utilized a 5 mm diameter air turbine, stable runs at 830,000 rpm were achieved. This paper concentrates on the design and manufacturing of the turbine/compressor/shaft assembly, and the evaluation of the compressor impeller performance by both experiment and from the results of CFD.

Some Design and Aerodynamic Performance Issues Related to Compressor and Turbine Size

Low Reynolds number, surface roughness, tip clearances, and minimum feature size are all important issues when one considers the design and performance of any miniaturized turbomachine. All four items can lead to reduced levels of performance, and thus require some discussion. Some guidance is found in the literature [4] concerning Reynolds number and surface roughness effects. Also, some very useful information may be obtained from papers on an earlier micro compressor (4 mm diameter at 500 m/s tip speed) even though the radial flow path is unusual: flat and two-dimensional [2, 5].

Scaling of efficiency for shrouded, radial flow compressor

impellers, typical of narrow industrial compressor stages, was established [4]. He used a Reynolds number based on tip speed, U_{tip}; blade height at the tip, b_{tip}; and kinematic viscosity at impeller inlet, which is $1.5 \times 10^{-5} m^2/s$ for air at room temperature and atmospheric pressure in the cases considered here. The method appears to work well when the flow through the impeller blade passages approximates turbulent flow in smooth and rough ducts.

The scale ratio is about 25:1 between this case, where b_{tip} = 1 mm, and a large scale, geometrically similar, high Reynolds number impeller where b_{tip} is approximately 1 inch. When Casey's scaling method is applied to impellers with tip speeds of 500 m/s, a reduction in stage efficiency by 11 % is obtained for hydraulically smooth surfaces. If the surface roughness height is 1 μm, an additional 3 points is lost.

It is noted that the Reynolds number for the small impeller is 3.35×10^4, which indicates that the flow in the impeller is turbulent, not laminar as it would be if the size were reduced by another factor of 10. The losses would increase catastrophically if the flow were laminar [5], and one may justifiably conclude that an impeller with a diameter of 1 to 2 mm may represent a lower limit, if efficiency is an important design criterion as it is here.

The current impeller does not have a rotating shroud like the impellers investigated by Casey. Here, there is no shroud cover, but an open clearance over the blade tips which is approximately 10 % of the blade height, b_{tip}. Thus the losses predicted above are not going to be better than rough estimates. Probably, the friction losses will be smaller, but there may be an additional loss due to leakage over the blade tips, which should increase as the clearance increases. This added loss, which is assumed to be independent of scale, was originally estimated to be 4 points in addition to other losses. Adding all losses together and assuming the design point efficiency of the micro compressor is 65 % says that a stage which is 25 times larger should have an efficiency of 83 %, a value in the expected range for this type of radial flow compressor. An attempt was made to determine the effects of change of axial clearance in the experimental program.

Finally, the effects of minimum feature size need to be discussed. Here, 0.3 mm (30 % of b_{tip}) was chosen as the blade thickness and the blade leading edges were not sharp as is the case in large high Mach number compressors of similar geometric shape. These effects will tend to increase blockage at both blade leading edges (inducer region) and at the trailing edges. There is currently no way to accurately estimate the added losses and separate them from the flow distribution (thicker boundary layers) blockage due to low Reynolds numbers. Blockage has several effects: (a) It reduces the flow area compared to the available geometric area and thus limits the through flow. This effect may be accounted for in design by an increase in dimensions such as b_2 when a particular mass flow rate is required. (b) Blocked area represents flow distortion which, compared to uniform flow, increases the mass-flow-average kinetic energy leaving the impeller. The downstream diffuser must cope with this non-uniformity as it reduces the kinetic energy and recovers it as static pressure rise. It is well known that increase of inlet blockage (flow distortion) leads to decrease in diffuser pressure recovery and consequently a loss in stage efficiency. In any case, the relatively large minimum feature size in the micro-scale compressor impeller is expected to have a negative influence on efficiency.

MICRO-SCALE CERAMIC COMPONENTS AND THEIR FABRICATION

Ceramics, especially silicon nitride, can have exceptional high temperature strength properties in a material of low density which makes them attractive for gas turbine applications where highly stressed turbines and other components must survive in contact with very hot gasses. In large turbines, vanes and blades are large enough to be manufactured with internal and film cooling which allows high temperature metals to be used in most cases. However, in the case of micro-scale turbines (diameter < 100 mm), the limits of scale preclude active blade cooling, and thus the blades must be solid which makes ceramics desirable, if they can be produced.

Two major issues have blocked application of ceramics to gas turbines, rotors in particular. The first is reliability and second is the lack of the shaping techniques. This project was able to avoid the reliability issue by noticing the increased reliability of the small sized ceramic components. The second issue has been overcome by the use of Mold SDM process with the application of gelcasting.

Reliability of Ceramic Components in Micro-Scale Gas Turbine Engines

The reliability issue is rooted on the brittle nature of the material. Figure 2 illustrates two characteristics of the fracture behavior of ceramic specimen under identical loading conditions. First, failure is sudden and complete, which is different from metal. Second, the maximum strength of each sample varies significantly in nominally identical specimens where Young's modulus is nearly constant. This characteristic, among others, points to flaws as the source of failure. Considering the brittle (sudden) failure mode, the biggest flaw contained in a specimen is responsible for the failure of the whole part.

Since the pore sizes follow a particular distribution, the size of the largest flaw tends to increase as the volume of the specimen increases under the same material and process condition. This property, accounted for in Weibull statistics, results in Equation 1. Here, V is the volume of the part of interest. The argument, m, of the function $f(m)$ is a parameter referred to as the Weibull modulus. σ_0 is a characteristic stress value for frac-

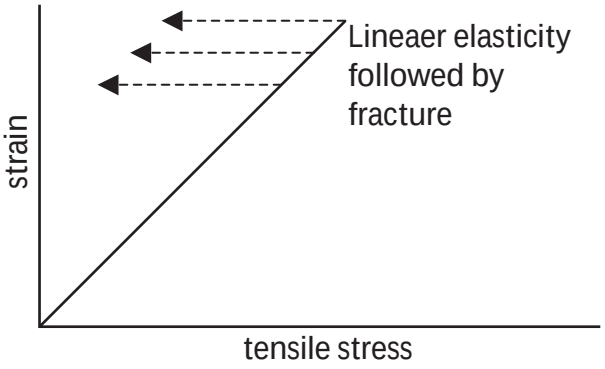

Figure 2. Fracture behavior of ceramic specimens under the identical loading conditions.

ture obtained by a statistical treatment [6]. The actual form of $f(m)$ varies according to the loading conditions. For example, $f(m) = 2(m+1)^2$ for three-point bending and $f(m) = 2(m+1)$ for four-point bending. In the actual design of a ceramic part, Equation 1 is used to calculate the allowable stress $\sigma_{\max}$ so that the part can have survival probability of P_s.

$$P_s = \exp\left[-\left(\frac{\sigma_{max}}{\sigma_0}\right)^m \frac{V}{f(m)}\right] \quad (1)$$

Since the argument of the exponential is negative, decreasing V (smaller volume) increases the P_s. A Taylor expansion of P_s around $P_s = 1$ shows that the failure probability P_f, which is defined as $P_f = 1 - P_s$, is proportional to V. This suggests the smaller the ceramic part, the more reliable [1].

Mold SDM Process

The Mold SDM process, a derivative of Shape Deposition Manufacturing (SDM) [7], combined with gelcasting one has the capability to fabricate silicon nitride components with full 3-D geometry containing features (e.g., blades) as small as 200 μm. It is even possible to achieve a complex monolithic geometry in a single part that is not possible with the conventional ceramic processes such as injection molding and green machining.

In the Mold SDM process, the fugitive mold of the final geometry is fabricated by SDM. SDM combines a material addition and material removal process to achieve both shape complexity and superior surface finish compared to the other rapid prototyping processes such as 3-D printing (3DP), stereolithography (SLA), selective laser sintering (SLS) and fused deposition manufacturing (FDM). Superior surface finish is particularly important in the fabrication of ceramic components since the strength of ceramic parts is highly sensitive to the surface smoothness due to the brittleness of ceramics.

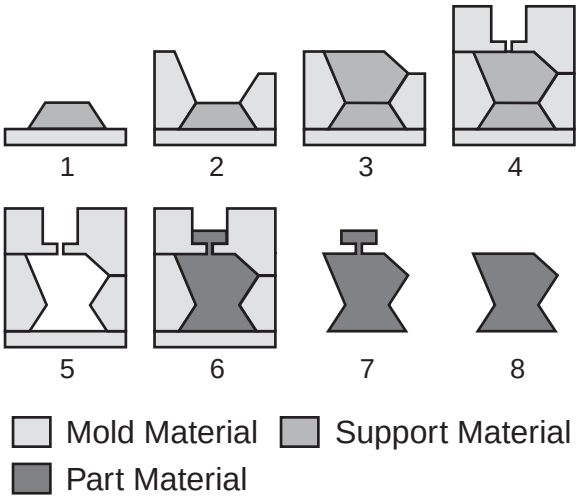

Figure 3. Mold SDM process build sequence example

Gelcasting is a ceramic forming process developed by Oak Ridge National Laboratory and is compatible with Mold SDM. Gelcasting slurry is a mixture of ceramic powder, monomers (chain former and branch former) and solvent. Usually, gelcasting slurries have low viscosity. Right before casting, an initiator system (a set of chemicals that initiates and propagates polymerization) is added. Then, the chain former and branch former contained in the slurry are transformed into polymer chains, which hold the ceramic particles in position and gives strength to the green part which is eventually sintered at high temperature to become the final, strong ceramic part.

Steps 1 to 4 of Figure 3 show the mold fabrication using SDM process. The mold and support materials are deposited by casting and shaped by machining. Since all the surfaces are directly shaped by machining or replicated from the machined surfaces, all the final geometry has the machined surface quality, which is about 1 μm RMS. Machinable waxes are used for the mold material and Aqua-Sol soldermask (Advanced Ceramics Research, Tucson, AZ) is used for the support material. Since the soldermask is UV curable liquid, it can be deposited into any shape. The solidified soldermask is dissolved in water leaving the cavity for the final geometry, as shown in step 5.

Silicon nitride gelcasting slurry is cast into the mold and cured (step 6) at an elevated temperature. Then follows the removal of the wax mold (step 7) by melting and removal of the casting features (step 8) completes the green part. The green part goes through ceramic processing such as drying (evaporation of the solvent) and removal of polymer chains and, finally, sintering at high temperature. During the sintering, the part densifies and obtains its full strength. A final part is shown in Figure 5.

Properties of Mold SDM Silicon Nitride

The strength of sintered ceramic components without any finishing (as-sintered strength) is smaller than that of the ground parts. The maximum strength of the sintered parts is achieved by grinding surface (polished strength) since it removes the surface layer and rough surfaces. Grinding, however, is not applicable to the Mold SDM ceramic parts due to their shape complexity. Thus, the as sintered strength, rather than the polished strength is more important to the Mold SDM ceramic parts. The Mold SDM silicon nitride specimens show mean strength higher than 400 MPa as long as the machined scallop height of the mold is under 5 μm [8]. The test sample size was $3 \times 4 \times 45$ mm and the silicon nitride composition was $8.6Y_2O_3 - 3Al_2O_3 - 88.4Si_3N_4$.

Table 1. The average strength values of Mold SDM silicon nitride measured in 4-point-bending at room temperature [8].

Material	Strength (MPa)
Si3N4 unpolished	414
Si3N4 polished	950
Si3N4 pressure sintering, polished	983

VERIFICATION OF THE DESIGN BY CFD AND EXPERIMENTAL METHODS

The aerodynamic performance of a compressor in a rotor group like the one shown in Figure 5 was 'tested' by two independent methods; (i) by direct measurements in a specially designed test facility, and (ii) by CFD analysis. The performance objective was to determine if the pressure ratio and efficiency at the design flow rate satisfied the requirements for ultimate, successful application in the gas turbine.

Test facility and procedures

The general goal was to verify the functionality of the compressor impeller at the highest possible rotor speed. No attempt was made to model the vaned diffuser planned for the gas turbine itself. The shaft of the rotor group fabricated with the Mold SDM process was mounted on two miniature ball bearings (3.175 mm ID) in an overhung position. The bearings were then mounted in a cartridge, held in an axial traversing unit that was actuated by a micrometer. Thus, the rotor group could be moved along the axis to vary the axial clearance between the blades and the fixed aluminum shroud, which also formed one wall of the radial vaneless diffuser. The opposite side of the diffuser and a downstream flow collection chamber were integral with a turbine inlet nozzle block, which included the turbine shroud and exit duct. This

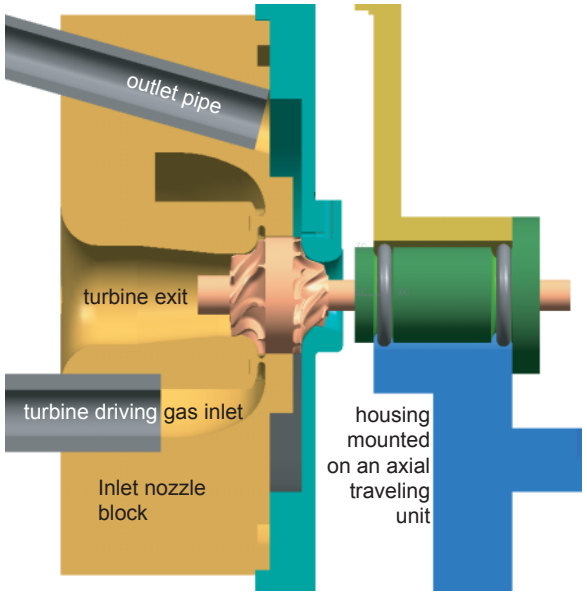

Figure 4. Cross section of inlet nozzle block, rotor group, bearings and mounting unit

complex part was fabricated in Ciba TDT 205-3 polyurethane by the SDM method, see Figure 4.

Flow entered the compressor impeller through a smooth bell mouth in the shroud wall. The four outlet pipes (only one shown above) from the collection chamber, downstream of the vaneless diffuser, were connected to a common tube. This tube passed into a flow meter (Sierra Instruments: Top-Trak 280 series, 0-150 SLPM) and a flow control valve which acted as throttle before the compressed air discharged to the atmosphere. Uncertainty of the flow measurement was $\pm 0.05\,\mathrm{g/s}$.

The turbine was driven by compressed, room temperature nitrogen supplied through four tubes inserted into a plenum chamber in the inlet nozzle block (only one shown in Figure 4). The turbine exit was to the atmosphere through a diffusing duct. Rotor speeds up to 500,000 rpm could be obtained with this system. Thus, testing at the design speed of 800,000 rpm was not feasible.

Rotational speed, N, was measured by a Fourier analysis of light reflected from one end of the shaft. The light was converted by an Optiphase Model V500 analog receiver. A National Instrument data acquisition board (PCI-MIO-16E-4) installed in a PC received the signal and the frequency was obtained by Fourier transformation performed with LabView software. Control of N to an accuracy of $\pm 1,200$ rpm was provided by regulation of the nitrogen pressure entering the turbine.

The densification of the silicon nitride during the sintering process is accompanied by linear shrinkage ($19 \pm 1\%$ in this case). This shrinkage is accounted for in the design before the molds are made. To satisfy final accuracy requirements, certain

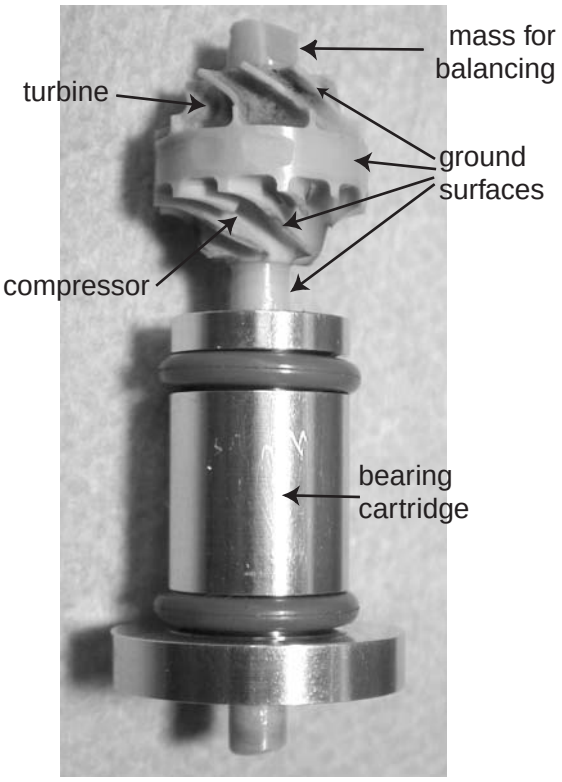

Figure 5. Rotor group mounted on ball bearings.

surfaces such as turbine and compressor blade-shroud-contour profiles, the outer tip diameter and the shaft of the rotor were ground to fine tolerances. The ground rotor was mounted on two bearings (hidden inside the cartridge) as shown in Figure 5. The rotor blades are much thicker compared to their span compared to those on larger rotors. No noticeable sagging of blades during sintering was observed.

The finite element analysis of the rotor at 800,000 rpm predicted that the maximum stress of 290 MPa will occur at the root of the compressor blade near the exducer. In this study, the life prediction using probabilistic code was not performed. Further investigation such as strength measurement at operating temperature is required to ensure a life time of rotor.

The rotor was balanced while mounted on the bearings to a residual unbalance of 0.003 g-mm static, 0.003 g-mm dynamic at 1,500 rpm. A combination of minute errors in rig machining and assembly combined with rotor vibrations when the rotor spins at high speed caused the speed limit of the rig to be 420,000 rpm to avoid short term mechanical failure. Since the test speed is only about a half of the design speed and the average strength value is higher than the predicted maximum value at design speed, proof tests were omitted.

Performance of this compressor rotor was therefore determined at a speed of 420,000 rpm by measuring the pressures and

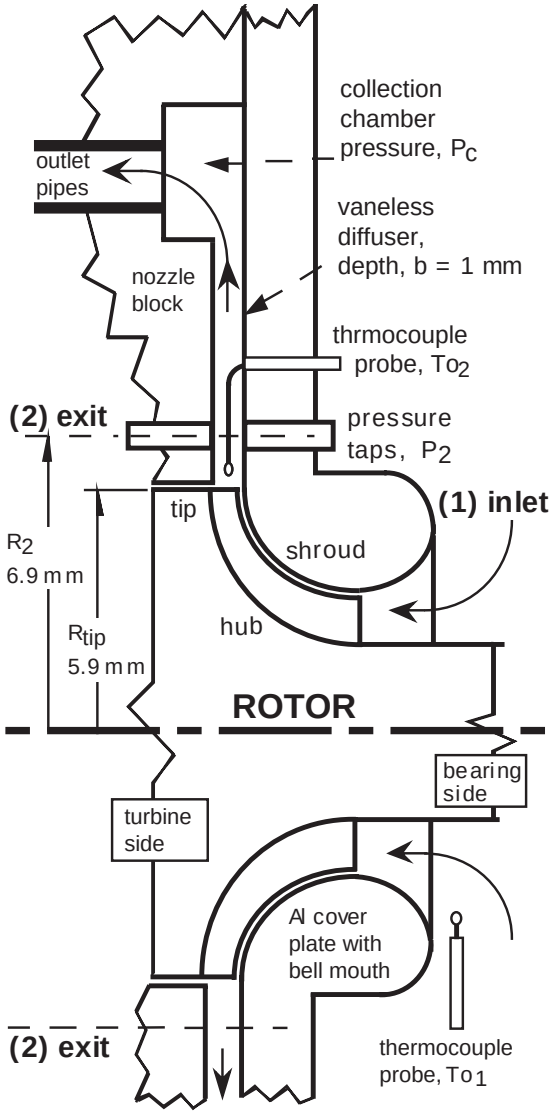

Figure 6. Compressor rotor in test rig showing measurement stations and instruments

temperatures at inlet and exit versus the mass flow rate, and by comparison to the results obtained by CFD. The small scale of the apparatus didn't permit detailed examination of the flow field leaving the impeller; only single point data at the exit (2) were possible. As a result, the mass flow average results obtainable from the CFD had to be compared to experimental results obtained using the assumption of one-dimensional, uniform flow at the exit (2) in the data analysis.

A cross section of the test rig is provided in Figure 6. This drawing is roughly to scale except for the collection chamber which is larger in the actual apparatus. The turbine rotor and nozzles, to the left, are not shown, nor are the bearings, which

are to the right in the Figure 6. Atmospheric air at (1) enters the inlet bell at very low speed, from the right. The exit state (2) for the impeller is measured at $R_2 = 6.9$ mm, a radius slightly larger than the tip radius of the impeller.

Four static pressures were measured: P_2, the exit static pressure, is the average of the pressures from the two wall taps at the exit station, (2). Only small pressure differences were observed between these taps. The pressure in the collection chamber, Pc, was indicated by pressure measured upstream of the metering valve. Pressure was also recorded from a forth wall tap (not shown) installed on the shroud side at $R = 6.185$ mm, but data from this tap was not considered reliable since a tap could not be installed at the same radius on the hub side. These pressures were measured to an estimated uncertainty of ± 6 kPa, on gauge pressure sensors by Omega (PX139-015D4V). Inlet pressure, Po_1, was taken to be 101.4 kPa, atmospheric pressure.

Temperature was measured at inlet (1) and exit (2) using type K thermocouples by Omega (5SC-TT-K-36-72), an ice reference and a precision multimeter. To_1, was obtained from a thermocouple placed near the inlet bell. At the exit station, the bare wires (0.127 mm dia.) were inserted through the a hole in the aluminum cover which forms the shroud wall, bent over in the radial direction with the junction set as close to the tip as possible, Figure 6. Between the hole in the cover and the junction, the bare wires comprised a 3 mm long stem. This was found necessary to avoid substantial conduction cooling of the junction by the Al cover which was always at about room temperature. To avoid aerodynamic interference, the radial thermocouple probe was displaced by 90 degrees relative to the circumferential location of the two wall static taps at (2). The overall uncertainty of the measured temperatures was estimated to be $\pm 1\,^{\circ}$C. Finally, data for each run was obtained only after the thermocouple readings had stabilized.

Special consideration was needed to obtain the stagnation temperature, To_2, at (2) because of the high speed of the flow (order 100 m/s) over the thermocouple probe. The raw readings were corrected by use of an aerodynamic recovery factor of 0.66 based on the tangential speed, V_t, in the location of the junction, which was very close to the tip of the impeller. The accuracy of this procedure is addressed below in the results section.

The desired final results, pressure ratio, (Po_2/Po_1), and the adiabatic efficiency, η, require the estimation of the exit stagnation pressure, Po_2, by application of the measured data. The assumptions are that air is a simple perfect gas, the velocity profiles at exit are uniform, and the flow fills the exit (no flow blockage). The flow speed at the inlet is nearly zero, so static and stagnation states are equal at (1).

The equations that were solved for the estimation of Po_2 are: Conservation of mass:

$$M_g = \rho_2 (2\,\pi\, R_2\, b_2)\, V_{r2} \tag{2}$$

Perfect gas equation of state:

$$\rho_2 = \frac{P_2}{R\,T_2} \tag{3}$$

Euler's turbine equation work = adiabatic, steady flow energy equation work input:

$$U_{tip} V_{t_{tip}} = C_p (To_2 - To_1) \tag{4}$$

Definition of stagnation temperature:

$$To_2 = T_2 + \frac{{V_{t2}}^2 + {V_{r2}}^2}{2C_p} \tag{5}$$

Estimation of V_{t2} by angular momentum conservation:

$$V_{t2} = V_{t_{tip}} \left(\frac{R_{tip}}{R_2} \right) \tag{6}$$

The solving these equations, after inserting the data, gives ρ_2, T_2, V_{r2}, $V_{t_{tip}}$, and V_{t2}, and thus:

$$Po_2 = P_2 \left(\frac{To_2}{T_2} \right)^{\frac{k}{k-1}} \tag{7}$$

$$\eta = \frac{To_1}{To_2 - To_1} \left[\left(\frac{Po_2}{Po_1} \right)^{\frac{k-1}{k}} - 1 \right] \tag{8}$$

Outline of the CFD method

The CFD code used here is based on a compressible-flow, Reynolds-averaged, Navier-Stokes method developed for computation of turbine and compressor rotor flows [9]. A low-Reynolds-number k-e turbulence model is incorporated, and the code uses structured, non-orthogonal, body-fitted meshes. For this case, one blade-to-blade passage was divided by the splitter into two primary streamtubes, which extended from inlet to just downstream of the exit in the vaneless space. The mesh sizes for the streamtubes were $196 \times 94 \times 49$. A clearance gap of 0.1 mm (10 % of b_{tip}) was incorporated in the computation. Computations were carried out at 800,000 rpm, the design-condition, and at test conditions, 420,000 rpm, so that direct comparison to the experimental results would be possible. Values of the properties at the exit (2) were obtained by mass flow averaging the detailed results.

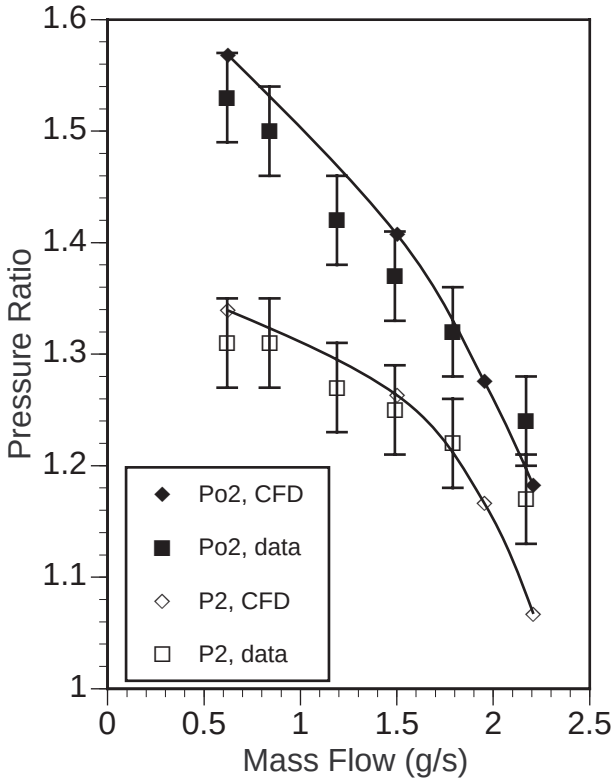

Figure 7. Pressure ratio at 420,000 rpm.

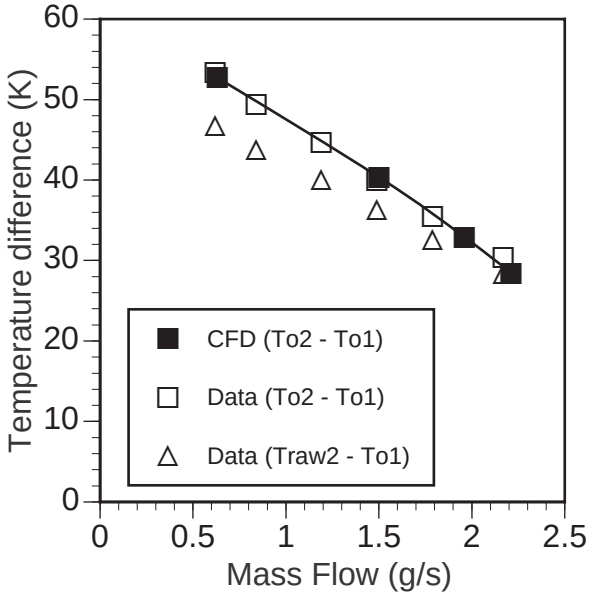

Figure 8. Temperature rise at 420,000 rpm.

EXPERIMENTAL AND CFD RESULTS

Pressure ratios and temperature differences were examined for consistency, and to check that the experimental results were reasonable because of the simplifying assumptions involved in arriving at the final results from the raw data. Figure 7 shows both data and CFD results for two pressure ratios, the static pressure ratio, P_2/Po_1, and the stagnation pressure ratio, Po_2/Po_1, plotted versus the mass flow rate at 420,000 rpm. The data based on the static pressure, P_2, is independent of the temperature data, and is shown in the lower set of points (open squares). The scatter in these points is less than with an estimate of the uncertainty [10] in the pressure ratio data, ± 0.06. The CFD results based on P_2, except for the point at highest flow rate, are in fairly close agreement with the measured results. The same conclusion may be drawn on comparison of the data and CFD results for Po_2, the solid points and curve in the upper portion of the graph. The method used to compute Po_2 from the raw data is also appears to be reasonable, but it also may contribute a small error to final results. It can't be concluded that either result is more accurate than the other because of significant differences between the two methods. For example, surface roughness effects, accuracy of blade angle settings at leading edges, axial tip clearances may all lead to small differences between experimental and CFD results.

Measured temperatures at the exit (2) and inlet (1) not only enter the estimation of Po_2 from the raw data, but they also are needed in the calculation of the adiabatic efficiency. The temperature rise (difference) enters directly in the denominator of the efficiency and its estimated uncertainty is about $\pm 1.5^{\circ}$C if proper corrections are made in the raw temperature readings. Figure 8 shows several results including probe data corrected for non-adiabatic effects. These data were very well correlated with the CFD results. $(T_{raw2} - To_1)$, based on direct, raw readings from the thermocouple at (2), gave low temperature rise values. Such low values led to efficiencies that were unbelievably high. Preliminary experiments with an exit thermocouple placed in the collection chamber gave even lower readings. This was thought to be the result of significant heat losses to the walls of the vaneless diffuser. Heat transfer effects can be a significant issue in a microscopic devices [2], and this is the reason that the exit thermocouple was placed as close to the impeller tip as possible.

Scaling of the pressure ratio results between different rotor speeds, in the case of slightly compressible flow, is accomplished by use of a dimensionless parameter, the flow coefficient, which in our case looks like, $M_g/(\rho_1 {R_{tip}}^3 \omega)$. For our purposes the inlet density and impeller tip speed are constant so a line of similarity which scales the mass flow rate, M_g, through the design point is

$$M_g = Mg_{dp}\left(\frac{\omega}{\omega_{dp}}\right) \tag{9}$$

The similarity line drawn on Figure 9 passes through the original design point at a pressure ratio of 3 and mass flow rate of 2.38 g/s for 800,000 rpm. It passes through the data for

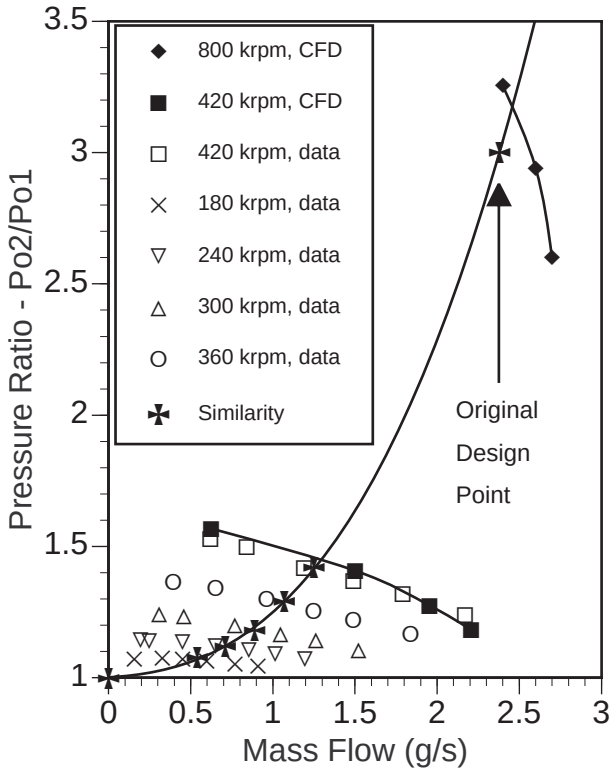

Figure 9. Pressure ratio at various rotor speeds with a curve of flow similarity.

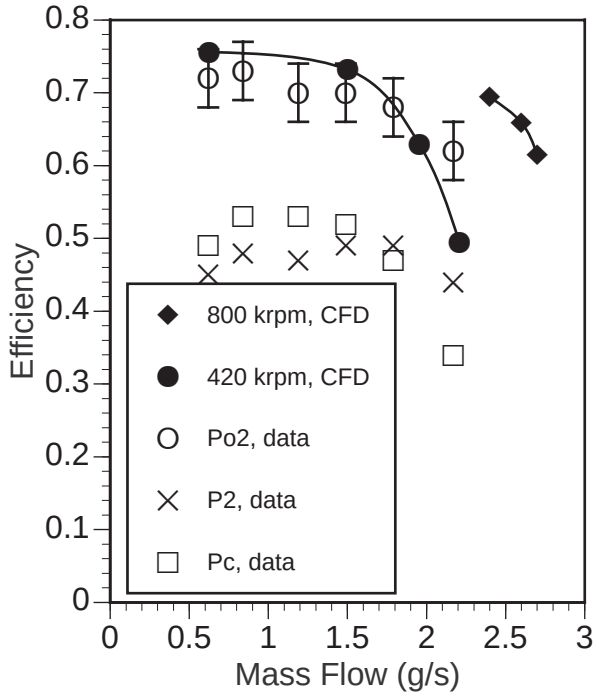

Figure 10. Adiabatic efficiency at 800 krpm and 420 krpm based on three pressures.

420,000 rpm at pressure ratio of 1.42 and mass flow of 1.25 g/s. Data for a number of lower speeds are also shown on the graph. The shape of the CFD curve at design speed has a slightly different shape from the curves at 420,000 rpm. This is because compressibility is much more important in this case, and simple similarity scaling cannot be expected to be exact. In particular, at the highest flow rate, local choking effects near the blade leading edges will cause a sharper downturn in the pressure ratio and efficiency. Later, in Figure 11, the effects of speed change on efficiency, along the design-point flow similarity curve, are presented.

The adiabatic efficiencies for 800,000 rpm and 420,000 rpm are compared in Figure 10. At the test conditions, the measured efficiency is about 0.04 points lower than the CFD results around the design-point similarity flow rate of 1.25 g/s. This could be significant even accounting for the estimated uncertainty. At high flow rate, the CFD result drops to lower values than is suggested by the data. Reasons for this are not known.

Two other sets of data were used in the calculation of the efficiency for 420,000 rpm to illustrate the need for a effective diffuser design. The first is based on the measured static pressure ratio, (P_2/Po_2), at the exit station, and the second on the pressure ratio from the downstream collection chamber (P_c/Po_1). Both these results show adiabatic efficiencies that are 0.24 and 0.18 points lower than the total-to-total (Po_2/Po_1) efficiency. To reduce the significant diffuser losses implied here, a very effective vaned diffuser design will be required for the actual compressor stage, not a simple vaneless space [5].

The efficiency was measured for a range of speeds from 420,000 rpm down to 180,000 rpm and it was found that the efficiency, in the region of the design point, at each speed increased, down to 240,000 rpm. Figure 11 illustrates this point and it includes the CFD results which end at the real design condition, 800,000 rpm. Also shown in the figure is the experimental uncertainty for the data. This indicates that the scatter indicated in the three low rpm points can be attributed to error in the data.

The uncertainty analysis used here [10] gives an estimate for single sample experiments based on a 95 % confidence limit. In the adiabatic efficiency, see Equation 8, the major contributions to error are the temperature rise $(To_2 - To_1)$ and the pressure ratio (Po_2/Po_1). The error in temperature at (2) is the major contributor to overall error at all speeds, but more so at lower speeds. In spite of the possible errors, a decrease in efficiency with increase in speed is a trend for this compressor impeller believed to relate to the increased sensitivity of the flow to compressible flow effects as rotor speed increases.

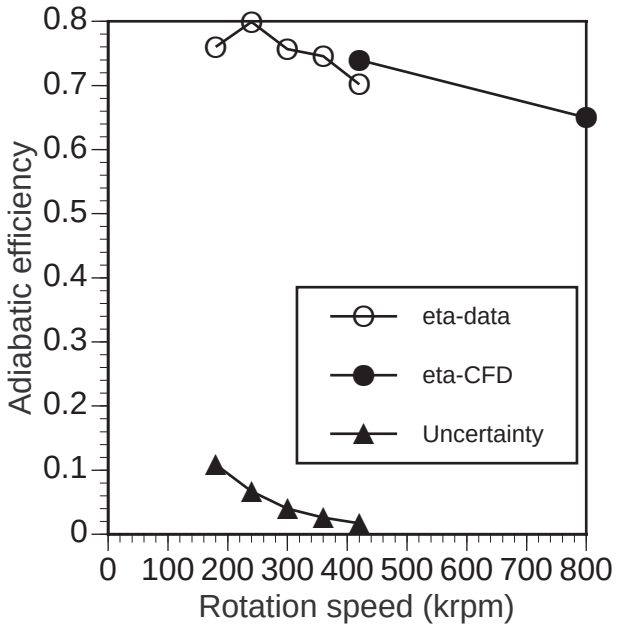

Figure 11. Adiabatic efficiency and its uncertainty versus rotor speed along a trajectory of flow rate similitude.

CONCLUSIONS

An essential element of a fist-sized, micro-scale, gas turbine engine, a monolithic, silicon nitride rotor (turbine-compressor-shaft), has been built successfully. The functionality of the compressor was confirmed by measurement of pressure ratio and adiabatic efficiency at 420,000 rpm and various flow rates. The successful test of the rotor group at high speed indicates the usefulness of Mold SDM process as the manufacturing process for the rotating components of micro gas-turbine engines.

The good match of experimental and CFD results suggests that current, preliminary design methods adapted to low Reynolds number conditions and combined with CFD techniques can be used to develop a micro-scale gas turbine engine with full 3-D shaped turbine and compressor impellers. However, tests confirming predicted performance at full operating speed, 800,000 rpm in this case, are still to be desired.

With the proper development of high-speed bearing technology, and the application of Mold SDM process for manufacture of the hot rotating elements in silicon nitride, a fist-sized micro-scale gas turbine engine appears to be a possibility.

ACKNOWLEDGMENT

We recognize Frank Holman and his team at M-Dot Aerospace in Phoenix AZ for their contributions in the preliminary design phases of this study. The contributions of Tibor Fabian, Tom Halser and Bernard Liu of Rapid Prototyping Laboratory at Stanford University in test rig design, assembly and rotor sintering are gratefully acknowledged. The support for ceramic processing by Atsushi Koizumi of Honda R&D Co., Ltd. is also greatly appreciated. Finally, we thank Professor Robert Moffat of Stanford University for his analysis and suggested solution for the temperature measurement problem.

REFERENCES

[1] Kang, S, 2002, “Fabrication of ceramic components for a micro gas turbine engine,” Ph.D. thesis, Stanford University, Stanford, CA.

[2] Epstein, A. H., et al., 2000, “Shirtbutton-sized gas turbines the engineering challenges of micro high speed rotating machinery,” Proceedings, 8th International Symposium on Transport Phenomena and Dynamics of Rotating Machinery, Honolulu, Hawaii.

[3] Isomura, K., et al., 2002, “Design of a micromachined gas turbine with 3-dimensional impeller,” Proceedings, 9th International Symposium on Transport Phenomena and Dynamics of Rotating Machinery, Honolulu, Hawaii.

[4] Casey, M. V., 1985, “The effects of Reynolds number on the efficiency of centrifugal compressor stages,” ASME Journal of Engineering for Gas Turbines and Power, **107**: pp. 541–548.

[5] Jacobson S. A., 1998, “Aerothermal challenges in the design of a microfabricated gas turbine engine,” Proceedings, 29th AIAA fluid Dynamics Conference, Albuquerque, NM.

[6] Wachtman J. B., 1996, *Mechanical Properties of Ceramics*, John Wiley & Sons, 1st ed..

[7] Cooper, A.G., et al., 1999, “Automated fabrication of complex molded parts using Mold Shape Deposition Manufacturing,” Materials and Design, **20**(2/3): pp. 83–89.

[8] Stampfl, J., et al., 2002, “Rapid prototyping and manufacturing by gelcasting of metallic and ceramic slurries,” Materials Science and Engineering A, **334**: pp. 187–192.

[9] Arima, T., et al., 1999, “A numerical investigation of transonic axial compressor rotor flow using a low-reynolds-number k-e turbulence model,” ASME Journal of Engineering for Gas Turbines and Power, **121**: pp. 45–58.

[10] Kline S. and McClintock F., 1953, “Describing uncertainties in single sample experiments,” Mechanical Engineering, **75**: pp. 3–8.